Hindawi Publishing Corporation
Journal of Sensors
Volume 2016, Article ID 4968476, 13 pages
http://dx.doi.org/10.1155/2016/4968476

Research Article

Indoor Operations by FMCW Millimeter Wave SAR Onboard Small UAS: A Simulation Approach

Antonio Fulvio Scannapieco, Alfredo Renga, and Antonio Moccia

Department of Industrial Engineering, University of Naples "Federico II", 80125 Naples, Italy

Correspondence should be addressed to Antonio Fulvio Scannapieco; antoniofulvio.scannapieco@unina.it

Received 6 January 2016; Accepted 17 March 2016

Academic Editor: Jian-Nong Cao

A dedicated system simulator is presented in this paper for indoor operations onboard small Unmanned Aerial Systems (UAS) by a novel millimeter wave radar sensor. The sensor relies on the principle of Synthetic Aperture Radar (SAR) applied to a Frequency Modulated Continuous Wave (FMCW) radar system. Input to the simulator are both design parameters for Synthetic Aperture Radar (SAR), which should be able to cope with the stringent requirements set by indoor operations, and information about platform navigation and observed scene. The scene generation task is described in detail. This is based on models for point target response on either a completely absorbing background or fluctuating background and ray tracing (RT) techniques. Results obtained from scene processing are finally discussed, giving further insights on expected results from high-resolution observation of an assigned control volume by this novel SAR sensor.

1. Introduction

Autonomous operations with small Unmanned Aerial Systems (UAS) indoors have been gaining interest in the last years [1]. Examples of these operations are indoor inspection in emergency missions, damage assessment or search for survivors in dangerous environments, and, more in general, dirty, dull, and dangerous activities in GPS-denied and substantially unknown environments. A Frequency Modulated Continuous Wave (FMCW) Synthetic Aperture Radar (SAR) operating in the millimeter wave represents an interesting solution to stringent time requirements due to autonomous navigation and mapping, size and power requirements, and range of environmental conditions [1, 2].

The choice of UAS as platforms to carry out these missions has an obvious advantage over ground-based robotic platforms [3, 4]; that is, motion of UAS is not limited to ground. However, this can be a disadvantage when dealing with complexity of algorithms to extract and exploit information from sensors.

In addition, reflections and diffraction phenomena could have strong impact on measurements when dealing with indoor and close-range radar applications, because multipath due to multiple reflections can occur in these scenarios. Therefore, data interpretation and analysis can benefit notably from the simulation of these physical mechanisms from both the geometric and radiometric point of view. Radiometric issues are handled in this work by taking into account a double-lobe scattering model [5], which is able to address both scattering and reflections from extended areas. Ray tracing (RT) algorithm is selected for dealing with geometric issues. Indeed, it follows a ray from transmission point to receiving point through resolution cells of the domain and allows the simulator to model reflection, refractions, and shadows [6]. Moreover, it also provides the users with information about ray intersection with other objects in the scene. RT algorithms have been exploited for analysis of several sensors, for example, laser [7], lidar [8, 9], radar [10–12], and applications, for example, scene rendering and indoor wireless net design [13–15]. With specific reference to SAR imaging, it is worth noting that SAR simulators have been typically developed under the assumption of parallel rays [10, 11], which is an adequate approximation for standard remote sensing applications. However, the assumption of

parallel rays is, in general, not valid for indoor applications due to short distances to travel. Hence, new approaches for indoor SAR raw data simulation are necessary.

The objective of present work is to develop a high-fidelity simulator for indoor raw FMCW radar data, assuming as a reference the interferometric SAR sensor proposed in [1]. The simulated data shall be then focused to achieve high-resolution SAR measurements. The sensor is assumed to be embarked on a small UAS to support indoor autonomous navigation and mapping operations. Hence, sensor dynamics are also part of the simulation. Outcomes of this work include the possibility of achieving a better characterization of this novel sensor, providing information on different levels, from achievable resolution in presence of not completely absorbing background to edge recognition. Obtained results are expected to support the definition of mission profile and strategies for future indoor autonomous UAS.

The work is organized as follows. Section 2 illustrates the simulation environment, the main characteristics, and the basic operating scheme. Section 3 provides the reader with relevant details of procedures for scene generation, for both point target analyses and ray tracing algorithms. Finally, Section 4 shows and describes the main results of simulations.

2. Simulation Environment

A simulation environment is the key element for analyzing the behavior of the sensor in envisaged scenarios. Figure 1 illustrates a schematic of the developed simulator and of its main blocks. The inputs, represented by white boxes, depend on radar design, selected scene, and navigation parameters. These data are given to the blocks that perform simulation steps, represented as gray squares in Figure 1. The "Scene Simulator" block is in charge of building the output raw signal from FMCW radar front-end observing the simulated scene and will be described in detail in Section 3. "Data processing" block, instead, performs SAR processing. It is worth noting that this block has been developed to read and process not only simulated but also real raw data, thus achieving focused SAR images and data for real scenery. Finally, white rounded boxes are the outputs of simulator, that is, raw data matrix, focused data matrix, and information about ambiguities in the scene [16].

As far as the inputs are concerned, each operational scenario can be conceived as a control volume that encloses platform and manifold targets. Dimensions of control volume depend on the application. A fixed reference system xyz, whose axes coincide with three main dimensions of control volume, is created. As for the targets, position and velocity are provided, as well as their radar cross section. It is worth noting that all targets are points and extended ones are simulated by increasing the number of point targets per resolution cell.

Design parameters depend on selected architectural scheme and mission requirements. Millimeter wave FMCW SAR has been selected in this work. This is because FMCW radars show interesting features for indoor operations [1, 16–20]. Continuous signal means less transmitted peak power because the duty cycle is one. Therefore, the power generation

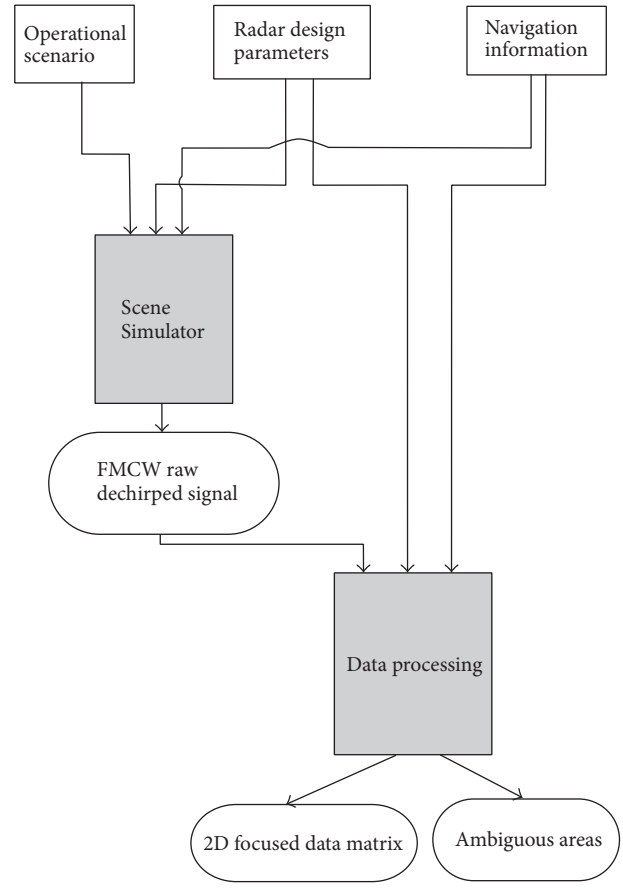

Figure 1: Schematic of simulator.

and conditioning unit can be made simpler and power requirements can be loosened with respect to traditional pulsed systems. In addition, thanks to deramp-on-receive technique [17], the signal to be processed, that is, the beat signal, has frequency proportional to range distance. Hence, the maximum bandwidth of beat signal depends on the largest observed range of distances. For close-range applications this leads to a bandwidth which is several orders of magnitude smaller than the transmitted bandwidth. Therefore, even GHz transmitted bandwidth can be easily handled by MHz sampling frequency. Also, frequency modulation allows obtaining range resolution equivalent to the one for conventional radar systems but range measurement for FMCW systems is obtained in frequency domain rather than in time domain. Hence, measuring the beat frequency allows retrieving instantaneously range, thus simplifying range gating. Finally, SAR choice enables improved resolution also in azimuth direction [21] even though it is necessary to handle Doppler effects due to continuous motion during transmission/reception of electromagnetic signal [1, 18].

Millimeter wave technology enables improvements in resolution both in range, due to a smaller ratio between transmitted bandwidth and carrier frequency, and in Doppler, due to smaller wavelength, directions, and hinders defocusing and smearing when dealing with moving targets. In addition,

Table 1: Design parameters.

Symbol	Parameter	Unit	Value
f_C	Carrier frequency	(GHz)	94
λ	Wavelength	(mm)	3.2
B	Transmitted bandwidth	(GHz)	1.50
f_S	Sampling frequency	(kHz)	165
PRF	Pulse Repetition Frequency	(Hz)	250
dr	Range resolution	(cm)	10
da	Azimuth resolution	(cm)	10
ρ_{MAX}	Maximum range	(m)	30
d	Antenna width	(cm)	1
θ_R	Antenna beamwidth in elevation	(°)	18
l_{AZ}	Antenna length	(cm)	2
θ_{AZ}	Antenna beamwidth in azimuth	(°)	9
P_T	Transmitted power	(mW)	<1

millimeter wave components typically show reduced dimensions with respect to other microwave elements. Finally, the signal experiences little attenuation through atmosphere and could pass through common obscurants like smoke and flames [16] in close-range operations. Therefore, this choice represents an ideal solution for fulfilling mission requirements set by dirty, dull, and dangerous indoor autonomous operations. It is worth noting that attenuation due to millimeter wave effects is not simulated in this paper, even though it can be taken into account when dealing with simulations of environments filled with smoke or flames. An example of design parameters is listed in Table 1. These values are relevant to the compact FMCW SAR system for UAS presented in [1], which is also able to look in every direction by reorienting the beam, and will be exploited in the remainder of this paper. The whole set of values has been derived by means of a design procedure for FMCW SAR: both mission requirements and expected mission profile for platform velocity and observation geometry have been used as inputs for the procedure [1]. In addition, it is worth noting that theoretical azimuth resolution is better than the one presented in Table 1: this has to be intended as the worst expected azimuth resolution, due to processing.

The last input block is represented by navigation information. This block provides the simulator with information about position, velocity, and attitude of the platform. In real operations, these data are provided by UAS navigation unit, which is connected to Processing Unit via direct interface data link [1]. It is worth noting that navigation data are also necessary to support image processing and data extraction.

Based on the receiver inputs, "Scene Simulator" generates the FMCW dechirped signal, which represents the raw signal necessary for data processing. The output is used as an input for "data processing" block. As shown in Figure 1 two outputs are available from "data processing" block. The first one is a 2D SAR matrix that can be stored and exploited for scene recognition and further interferometric processing [1]. The focusing method can be selected among four algorithms, that is, Back-Projection Algorithm (BPA), Range-Doppler Algorithm (RDA), Wavenumber Domain Algorithm (WDA), and Frequency Scaling Algorithm (FSA). The standard implementation of these algorithms, that is, the one concerning pulsed radar operation, has been extended to an FMCW architecture following the results presented in [22–25]. The second output is represented by information on ambiguous areas that could be observed during flight trajectories. The gradient method [26] is used to individuate ambiguous areas, that is, all the areas of the control volume which cannot be observed with the desired resolution at certain time and platform location or during a complex trajectory [1, 16]. This output is necessary because, as noted above, envisaged missions, differently from most of conventional remote sensing applications, require the system to observe scene along directions that could be not perpendicular to the motion of platform, that is, regions in which image resolution can be degraded notably. Hence guidelines for trajectory optimization and mission profile can be drawn.

3. Scene Generation

The scene generator is the most important block as it reproduces the FMCW raw radar signal of an envisaged scenario. In the following three main subblocks will be described. They have been developed to provide analysis of performance even in presence of fluctuating targets and basic understanding of echoes in presence of possible indoor multipath.

3.1. Point Target Analysis. The choice of FMCW technology for novel radar system results in processing of beat signal [17] to obtain meaningful information about the scene. For a quasi-monostatic setup, that is, a setup in which transmitting and receiving antenna are not physically located in the same position but the operational distance is so that a monostatic configuration approximation is valid, and neglecting effect of signal amplitude, a point target at distance ρ is described by the beat signal

$$s_B(t) = \mathrm{rect}\left(\frac{t-\tau}{T}\right)\exp\left\{2\pi j\left(f_C\tau + \frac{B\tau}{T}t\right)\right\}, \quad (1)$$

where t is the time, T is the sweep duration, the time delay due to distance is $\tau = 2\rho/c$, and c is the light velocity. In (1) Residual Video Phase (RVP) contribution [19] has been neglected. When multiple point targets are addressed, (1) becomes

$$s_B(t) = \sum_{i=1}^{M}\mathrm{rect}\left(\frac{t-\tau_i}{T}\right)\exp\left\{2\pi j\left(f_C\tau_i + \frac{B\tau_i}{T}t\right)\right\}, \quad (2)$$

where M is the number of point targets [19].

The "Scene Simulator" block rearranges signals (1)-(2) in a 2D complex-value matrix, whose ith row represents echoes corresponding to ith transmitted sweep. This is performed assuming colocated Tx and Rx antennas.

It is worth noting that the line-of-sight, or boresight, $\hat{\mathbf{l}}$ is obtained in the fixed reference xyz from the knowledge of platform attitude and observation geometry by means of products of rotation matrix. Indeed, the observation

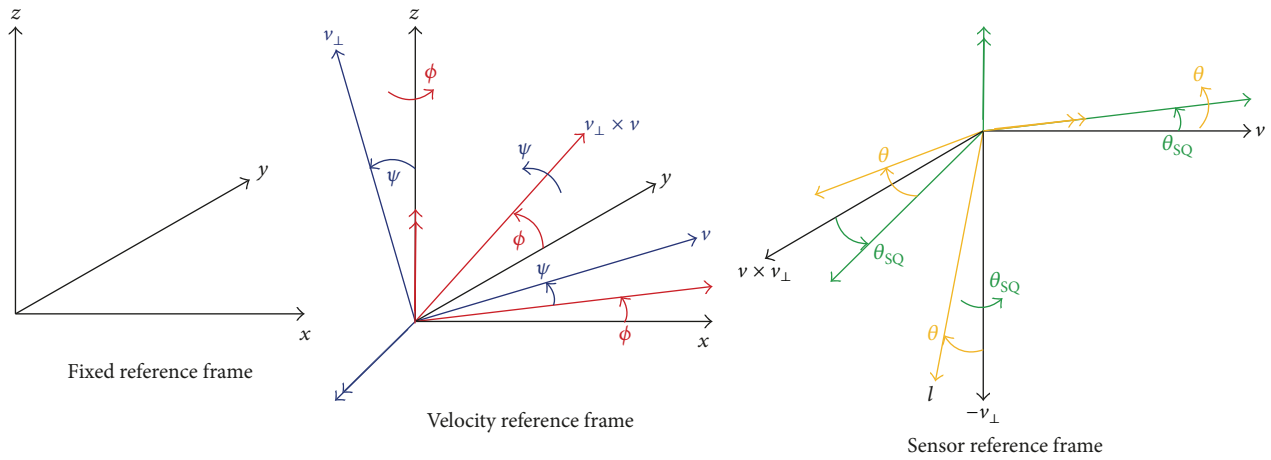

(a) Reference frames and rotations

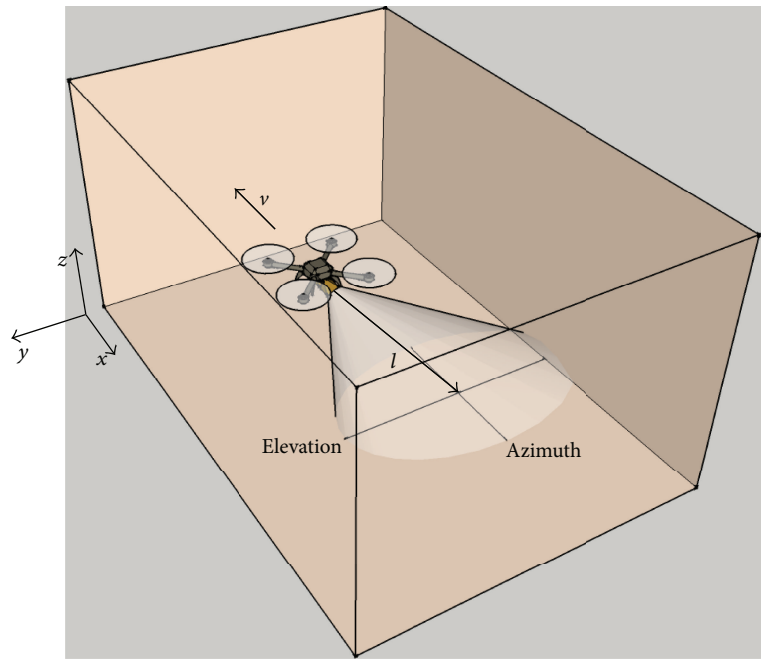

(b) 3D view of analyzed scenario

Figure 2: Schematics for simulated operations.

geometry represents the relative attitude of antennas with respect to platform. Therefore, the explicit expression for $\hat{\mathbf{I}}$ is

$$\hat{\mathbf{I}} = \begin{bmatrix} -s(\theta_{SQ})\, s(\theta)\, c(\psi)\, c(\varphi) - c(\theta_{SQ})\, s(\psi)\, c(\varphi) - s(\theta_{SQ})\, c(\theta)\, s(\varphi) \\ c(\theta_{SQ})\, s(\theta)\, c(\psi)\, c(\varphi) - s(\theta_{SQ})\, s(\psi)\, c(\varphi) + c(\theta_{SQ})\, s(\varphi)\, s(\theta) \\ s(\theta)\, s(\varphi) - c(\theta)\, c(\psi)\, c(\varphi) \end{bmatrix}, \tag{3}$$

where $c(\cdot)$ and $s(\cdot)$ represent cosine and sine functions, θ is off-nadir angle, θ_{SQ} represents squint angle, and φ and ψ are the pitch and heading angle, respectively. Figure 2(a) shows reference frames and angles, whereas Figure 2(b) illustrates the analyzed scenario.

In order to model a fluctuating point target it is necessary to introduce image speckle. The implemented approach simulates extended targets, like background, as more point targets in a single resolution cell [27]. In addition, the beat signal (2) is modified to account for the

Table 2: Set of basic actions required in 2D RT algorithm.

Identifier	Normal vector	Action
0	Null	Keep on propagating
1	$\hat{\mathbf{n}} = [1; 0]$	Compute new direction and increase hit counter
2	$\hat{\mathbf{n}} = [-1; 0]$	Compute new direction and increase hit counter
3	$\hat{\mathbf{n}} = [0; 1]$	Compute new direction and increase hit counter
4	$\hat{\mathbf{n}} = [0; -1]$	Compute new direction and increase hit counter
5	$\hat{\mathbf{n}} = \left[\frac{1}{\sqrt{2}}; \frac{1}{\sqrt{2}}\right]$	Compute new direction and increase hit counter
6	$\hat{\mathbf{n}} = \left[-\frac{1}{\sqrt{2}}; \frac{1}{\sqrt{2}}\right]$	Compute new direction and increase hit counter
7	$\hat{\mathbf{n}} = \left[-\frac{1}{\sqrt{2}}; -\frac{1}{\sqrt{2}}\right]$	Compute new direction and increase hit counter
8	$\hat{\mathbf{n}} = \left[\frac{1}{\sqrt{2}}; -\frac{1}{\sqrt{2}}\right]$	Compute new direction and increase hit counter
9	$\hat{\mathbf{l}}$	Stop ray

statistical properties of amplitude and phase of the background

$$s_B(t) = A\,\mathrm{rect}\left(\frac{t-\tau}{T}\right)\exp\left\{2\pi j\left(f_C\tau + \frac{B\tau}{T}t\right)\right\} + \sum_{i=1}^{M_B} A_i\,\mathrm{rect}\left(\frac{t-\tau_i}{T}\right)\exp\left\{2\pi j\left(f_C\tau_i + \frac{B\tau_i}{T}t\right) + \phi_i\right\}, \quad (4)$$

where A_i follows a Rayleigh distribution, depending on clutter RCS and varying on a pulse-by-pulse basis, and ϕ_i is a uniform phase distribution in $[0, 2\pi]$ [27]. It is worth noting that, following traditional SAR and radar literature, statistical distribution is valid only for background, whereas point targets not representing background have deterministic amplitude and phase.

3.2. 2D Geometry. The first step towards understanding the effects of indoor scattering and reflection phenomena on radar returns is a two-dimensional simulation, that is, a simulation in which echoes coming from points at different azimuth position with respect to the antenna are neglected. Indeed, even though this is not a real case, it will be shown that it helps in defining geometries and analyzing system behavior.

The core of this block is an adaptation of the ray tracing algorithm proposed in [6], which is restricted to y-z plane. It is clear that with the same approach even x-y and x-z planes can be analyzed. A grid is created and the size of each cell of the grid is set as an input parameter. In the present implementation, each cell is a square and the grid is uniform but either different sampling steps for each direction or nonuniform grid distribution can be easily implemented. It is worth noting that size of cell should be smaller than expected resolution for realistic simulations. The origin of the rays is the center of the transmitting antennas and the rays are uniformly distributed around the line-of-sight direction $\hat{\mathbf{l}}$ and within the beamwidth θ_R. It is worth recalling that the assumption of parallel rays [10, 11] is not used in this work owing to short distances to travel when dealing with indoor applications.

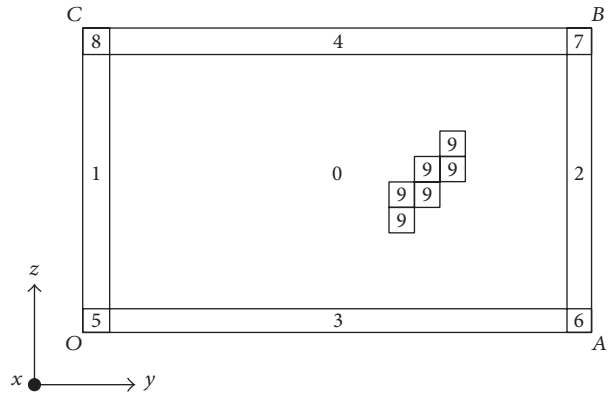

Figure 3: Schematic of 2D grid values. Areas associated with value 0 represent the propagating medium; cells having values ranging from 1 to 8 are the walls. Receiving antenna is represented by value 9. Size of grid cells with respect to total size of grid is not to scale, for clarity.

Objects in the scene are modeled by assigning specific parameters to the cells whose position in the grid corresponds to position of the objects. The elements which are always present in the grid are the walls, the antennas, and the propagating medium. As shown in Figure 3, each of them is identified by an integer number, corresponding to both different values of normal vector and action required. Actions and normal vectors are listed in Table 2. It can be seen that if the ray is in the cell corresponding to the propagating medium, air in the present work, then there is no normal vector and the ray is free to travel along its path. On the contrary, if the ray reaches a cell corresponding to a wall, specular reflection mechanism is enabled. In particular, the direction $\hat{\mathbf{r}}$ of reflected ray is found according to the formula

$$\hat{\mathbf{r}} = \frac{\hat{\mathbf{d}} - 2\left(\hat{\mathbf{d}}\cdot\hat{\mathbf{n}}\right)\hat{\mathbf{n}}}{\left|\hat{\mathbf{d}} - 2\left(\hat{\mathbf{d}}\cdot\hat{\mathbf{n}}\right)\hat{\mathbf{n}}\right|}, \quad (5)$$

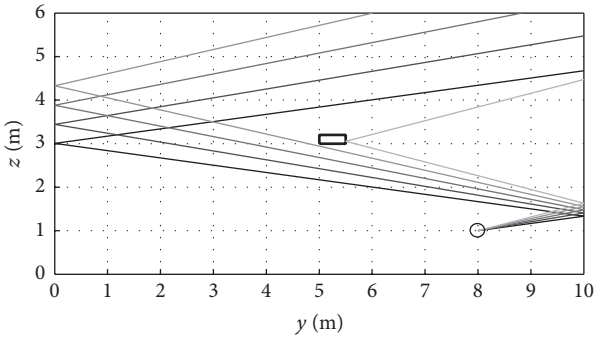

Figure 4: Example of reflections due to an object (rectangle, bold) in the scene. Position of antennas is revealed by black circle.

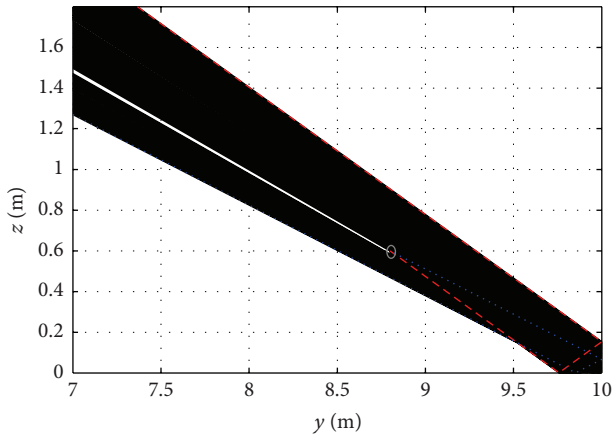

Figure 5: 2D geometry: example of rays intercepted by receiving antenna. Transmitting and receiving antennas are oriented towards the bottom-right corner and gray circle shows their location. Blue dotted and red dashed rays indicate the borders of transmitted beam, whereas inner rays are depicted in black. The energy is reflected back to both the antenna and the top-left corner: some rays hit the antennas, and hence they are not propagated towards the top-left side of the grid (transparent area). The figure represents a detail of the total grid.

where $\hat{\mathbf{d}}$ is the direction of the impinging ray and $\hat{\mathbf{n}}$ is the direction normal to the considered surface. Similarly, reflection on a random object in the scene can be simulated by association with normal vectors to cells, as shown in Figure 4. It is worth noting that the simulator counts how many times a ray hits either a wall or an object within the scene. The maximum allowable number of hits, N_{HITS}, before halting the ray is directly related to the number of specular reflections, $N_{\text{REFLECTIONS}}$, by the simple equation

$$N_{\text{REFLECTIONS}} = N_{\text{HITS}} - 1. \tag{6}$$

The assumption of two specular reflections has been formulated, so that the number of hits is three. This assumption derives from the observation that after three bounces the signal has lost most of its power owing to absorption and spread of energy. Finally, in order to model antenna effect, when the ray hits a cell filled with antenna identifier the ray itself is always halted; also, the reflection is received by the antenna only if the direction is within the beam of radar, that is,

$$\hat{\mathbf{l}} \cdot \hat{\mathbf{r}} < -\left|\cos\left(\theta_R\right)\right|, \tag{7}$$

where the sign "–" is due to the fact that line-of-sight and ray directions have opposite verse when the ray impinges on the antenna. Figure 5 shows a set of rays stopped by the antenna: in general, owing to the divergence of rays, the smallest the distance travelled by the rays when hitting the antenna is, the largest the number of them whose path is blocked is.

It is worth noting that diffraction phenomena can be modeled, too [28].

A relevant role in the proposed simulator is also played by radiometric effects. Indeed, once the geometric paths have been set, it is necessary to simulate how much energy is associated with diffusion, reflection, and absorption by the scatterer. In general, a geometric definition of reflectance factor R by means of reflectance function, also called Bidirectional Reflectance Density Function (BRDF), requires the knowledge of the variation of BRDF itself with impact point and directions of both incident and scattered rays [29]. In addition, this value depends on several other parameters. The first one is the polarization of emitted wave: indeed, depending on the direction of polarization, different equations for reflectance factor are provided and R can also become equal to zero in correspondence with Brewster's angle [7]. Then, the wavelength could significantly change reflectance values, especially when dealing with materials with strong internal scattering [29]. Surface roughness has also a role in scattering phenomena as when it is not negligible when compared with the wavelength of the incident rays, the energy is scattered more in millimeter wave than at lower frequencies [13].

Several models exist for simulating the radiometric behavior of different kinds of environments [12, 13, 30, 31]. The one hereby adopted is an adaptation of double-lobe model proposed in [5], which has been used for taking into account realistic diffusive phenomenology in RT. The adaptation lies in the fact that a single ray is supposed to be scattered from the point where the incoming ray impinges, instead of a fan of rays.

In detail, when the transmitted ray hit the surface the power balance is

$$1 = \frac{P_L}{P_i} + \Gamma^2\left(S^2 + R^2\right), \tag{8}$$

where P_L is the power loss due to absorption/transmission and P_i is the incident power, S is the scattering coefficient with respect to reflected energy, R represents the reflection reduction factor coefficient, and Γ^2 represents the reflected power with respect to incident power. The ratio P_L/P_i is the transmission loss and depends on the wavelength, on the material of walls, and on roughness, too.

Incident power can be described as

$$P_i = \frac{1}{4\pi\rho^2} G_T P_T \sigma \tag{9}$$

ρ being the distance, G_T the transmitting antenna gain, P_T the transmitted power, and σ the radar cross section (RCS).

Therefore, the scattering coefficient can be computed as

$$S = \sqrt{1 - R^2}. \tag{10}$$

In addition, according to the double-lobe model [5], here reported for the sake of clarity, scattered energy can be described as

$$E_S^2 = E_{S,0}^2 \left[\Lambda \left(\frac{1 + \cos \psi_B}{2} \right)^{\alpha_B} + (1 - \Lambda) \left(\frac{1 + \cos \psi_F}{2} \right)^{\alpha_F} \right], \tag{11}$$

where $E_{S,0}$ is the maximum scattered energy, Λ is the percentage of backscattered energy, ψ_B and ψ_F represent the difference between angle of back-specular and forward-specular scattering and the actual ray direction, and α_B and α_F are factors that take into account the size of the beams. Scattering factor S is within the definition of maximum scattered energy. With the aforementioned approximation a quantity Λ of the whole scattered energy is given to backscattering contribution whereas the remaining $(1 - \Lambda)$ amount and reflected energy are assigned to reflected rays. In addition, a further parameter is multiplied by the reflected energy, that is,

$$L_{\mathrm{RX}} = \frac{N_{\mathrm{REFLECTED}}}{N_{\mathrm{RAYS}}} \tag{12}$$

which represents the amount of reflected energy that reaches the receiving antenna, due to ray divergence.

It is important to note that no backscattering returns coming from second and third hits are considered in this simulation. This approximation is due to the fact that the walls are supposed to have a uniform and very low radar cross section; therefore, the energy backscattered from points hit by reflected rays is negligible. This issue will be further discussed in Section 4.2. However, if bright targets, showing a larger value of RCS, are present in an actual scene, this approximation could not be valid. Indeed, ghost signatures due to multiple backscattered reflections from bright target not in line-of-sight could appear in the image, as in [32], thus causing misleading interpretation of the image itself.

Finally, it is worth highlighting that even though it is available in the framework of the simulator, fluctuating model has not been applied to 2D and 3D analyses as the principal objective is to assess dominant element in a uniform scene.

3.3. 3D Geometry. The 3D RT simulator is the natural extension of two-dimensional techniques discussed in previous subsection. In detail, azimuthal components are enabled and squint-looking observations are allowed. Again, it is possible to set dimensions of grid voxels to be both uniform and nonuniform and reflections in the domain are computed according to (4), even though the list of identifiers takes into account surfaces besides edges and vertices. It is worth noting that the set of actions for modeling reflections by (5) now is more complex as it handles also beamwidth in azimuth. Figure 6 shows a 3D scene with ray reflections scene.

Table 3: Dimensions of control volume.

x (m)	y (m)	z (m)
30	10	6

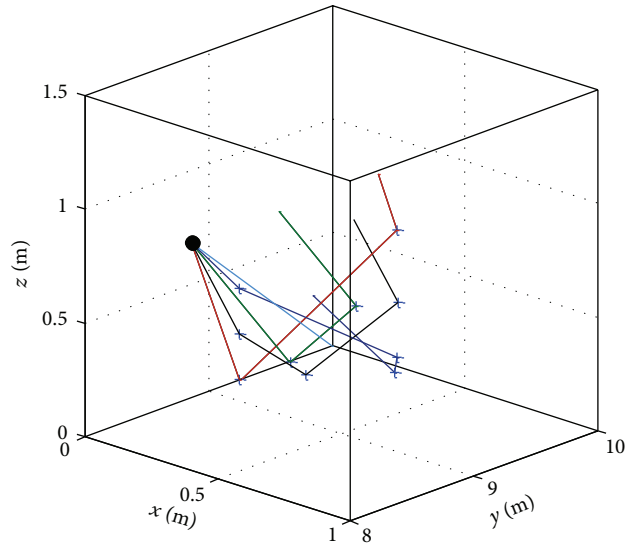

Figure 6: 3D view of reflected rays: black dot represents the position of antennas; blue crosses are the points where reflection occurs. Only a small part of the whole control volume is shown, for clarity.

For 3D simulations, rays are emitted for each position occupied by the Tx antenna during the synthetic aperture. Hence, a proper simulation of FMCW SAR raw signals has to be accounted for. In addition, as it is possible to observe multiple reflections from trihedral corners, the maximum number of reflections has been raised to three.

4. Results

4.1. Point Target Analysis. In this section, great attention will be paid to results for fluctuating target analysis. A detailed discussion about point scatterers on completely absorbing background in the same scenario is reported in [19]. The dimensions of control volume adopted in present work are listed in Table 3. A point target at position $T_P = [15.0, 8.0, 0.0]$ (m) is imaged, with the platform initially located at $P_0 = [14.8, 1.4, 4.5]$ (m). The platform is observing scene in side-looking mode and moves at constant speed $v = [0.5, 0.0, 0.0]$ (m/s). Each cell contains at least 9 point targets representing background. For the sake of simplicity, a unit radar cross section σ has been selected for the point target, whereas two different mean radar cross sections have been selected for background, respectively, 10 dB and 20 dB smaller than that of the point target. Histograms showing occurrences of amplitude values for a single pulse are depicted in Figures 7(a) and 7(b), whereas the phase is shown in Figure 7(c).

Tables 4 and 5 list the focusing results of the four implemented algorithms for a background having −20 dB and −10 dB intensity, respectively. Performance in terms of Impulse Response Width (IRW), Peak Sidelobe Ratio (PSLR),

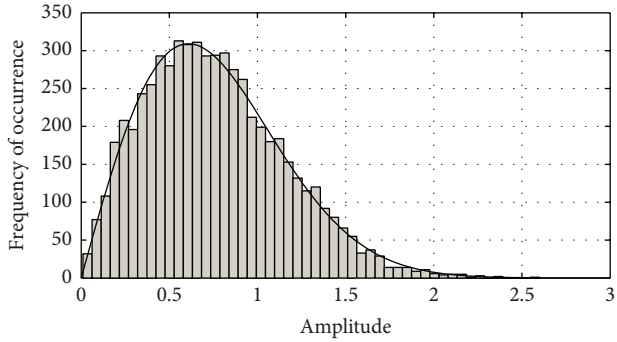

(a) Histogram showing Rayleigh distribution of amplitude for a cell having uniform background at $\sigma = -10$ dB and for a single sweep

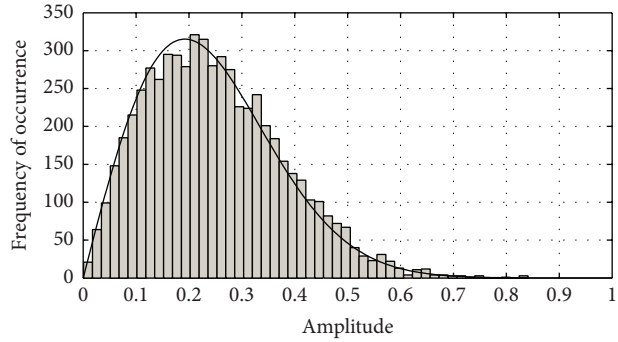

(b) Histogram showing Rayleigh distribution of amplitude for a cell having uniform background at $\sigma = -20$ dB and for a single sweep

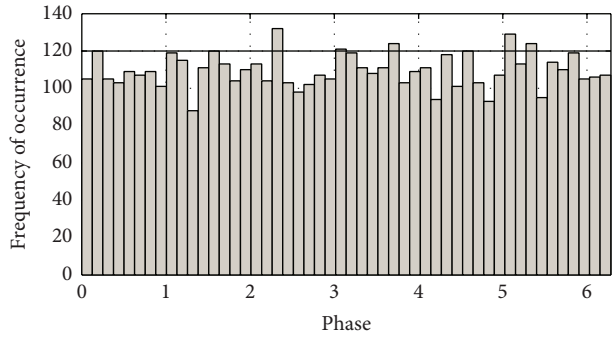

(c) Histogram showing uniform distribution of phase for a cell having uniform background and for a single sweep

Figure 7: Fluctuating target: examples of amplitude and phase distribution.

Table 4: Fluctuating target: point target on −20 dB background.

	IRW (bins)		PSLR (dB)		ISLR (dB)	
	Mean	Variance	Mean	Variance	Mean	Variance
BPA	0,865	0,006	−13,192	0,269	−10,686	0,134
	0,823	0,003	−12,682	0,298	−9,695	1,054
WDA	0,887	0,004	−13,102	0,244	−10,217	0,134
	0,809	0,003	−12,670	0,272	−10,258	0,141
RDA	0,883	0,004	−13,145	0,248	−10,335	0,132
	0,799	0,003	−12,632	0,270	−10,037	0,341
FSA	0,887	0,011	−12,925	0,216	−10,571	0,153
	0,841	0,005	−11,615	0,233	−9,600	1,035

Table 5: Fluctuating target: point target on −10 dB background.

	IRW (bins)		PSLR (dB)		ISLR (dB)	
	Mean	Variance	Mean	Variance	Mean	Variance
BPA	0,859	0,081	−10,195	1,850	−6,636	1,309
	0,832	0,020	−9,905	1,312	−3,625	3,356
WDA	0,874	0,038	−10,104	1,839	−5,604	1,268
	0,807	0,033	−10,414	1,356	−5,818	1,287
RDA	0,878	0,053	−10,284	1,887	−5,924	1,213
	0,809	0,020	−10,589	1,264	−4,982	1,551
FSA	0,873	0,112	−9,691	1,952	−6,125	1,338
	0,809	0,043	−7,068	3,105	−5,395	1,533

and Integrated Sidelobe Ratio (ISLR) is shown for each algorithm. Specifically the first and the second row refer to the performance in range and azimuth direction, respectively.

Results show that, in the considered scenario, fluctuations do not affect IRW. In addition, a −20 dB background gives results similar to the ones for completely absorbing background in [19]. This result suggests that further simulations can be carried out considering point targets only. On the contrary, a background with stronger intensity raises sidelobes level and energy of about 3 dB. This can be seen also in Figures 8 and 9 where BPA results are depicted: depending on the actual realization of the statistical distributions, cases exist in which some peak lobes can be even higher than −10 dB.

4.2. 2D Geometry. A proper set of parameters able to model the observed scene is necessary to implement both RT and double-lobe model properly. In more detail and as discussed in Section 3.2, the capability of a surface either to scatter or to absorb the incidence energy depends on several parameters, including surface roughness, material, signal wavelength, and polarization. In the present example, transmission loss and reflection coefficient are set to −7.0 dB and −7.5 dB, respectively. These values are representative, in millimeter wave region, of walls made of concrete [13]. In addition, $\Lambda = 0.1$ is chosen by considering that, in general, backscattered energy is lower than the amount scattered along and around specular direction. This value leads to an energy level of

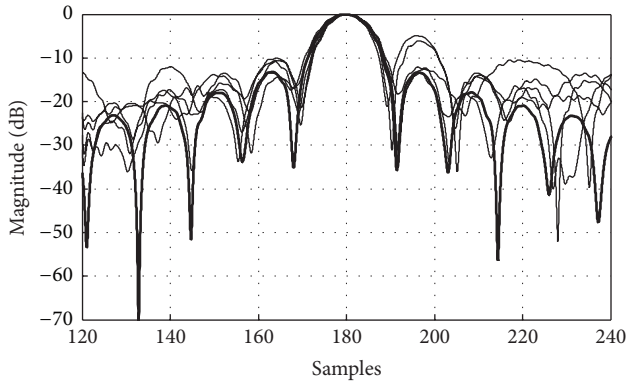

Figure 8: BPA −10 dB range. 5 realizations. Nominal condition, that is, point target on absorbing background, in thick black line.

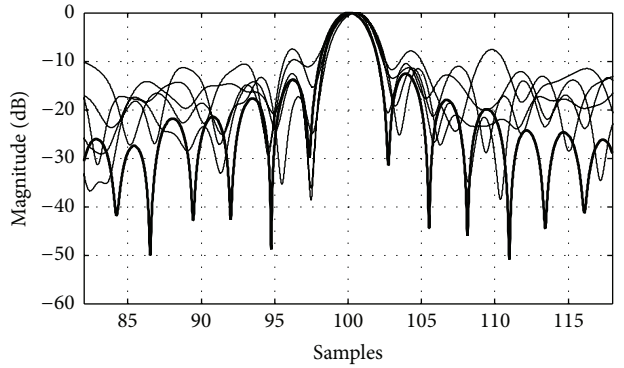

Figure 9: BPA −10 dB azimuth. 5 realizations. Nominal condition, that is, point target on absorbing background, in thick black line.

backscattering returns coming from second and third hits at least 9 times lower than energy level from multiple reflections, thus making the approximation presented in Section 3 acceptable. The selected radar system presented in Section 2 has been designed considering $\sigma^0 = -20$ dB [1]; therefore, that value has been kept even in the present section. Moreover, in order to analyze the effects of reflections, simulations are conducted with backscattering effects only and backscattering plus reflections. In addition, it is worth highlighting that uniform wall has been modeled by locating several point targets on absorbing background in each cell, and the number of point targets depends on the number of rays. Overall, 300 rays have been used in the two-dimensional simulation.

Two different cases are analyzed. The first case is depicted in Figure 10. The antenna is at position $P_0 = [8.8, 0.6]$ (m) and the off-nadir angle, θ, is 57° (see plots in Figures 10(c) and 10(d), resp.). The reflected rays are not incident on the antenna, so that the difference in amplitude between backscattered echoes and complete echoes is zero (see plot in Figure 10(b)). The echoes coming from the scene (Figure 10(a)) show a higher peak shifted towards the boresight direction (indicated as Center Scene, CS) followed by a smaller one corresponding to Far Range (FR): this is mainly due to the accumulation of targets in the Near Range (NR).

The second case considers the antenna located at $P_0 = [8.0, 1.0]$ (m) that is farther from the wall than in the previous case. The off-nadir angle is 60° in this second case. The results are depicted in Figure 11. The reflected rays (Figure 11(a)) hit back the antenna and generate a small contribution (Figure 11(b)) in distribution of echoes. The variation of amplitude given by incoming reflected rays is about four orders of magnitude lower than amplitude due to backscattering. This result could be explained by observing that the parameter (12), which accounts for divergence of rays, is much smaller than unit. It is worth noting that the peak of reflected energy is in range bins corresponding to the area of backscattering returns. This could be expected as the geometry is the one of a corner reflector. Concerning the peak shifted towards FR, this is due to layover [20] and not to reflected rays.

The results obtained by 2D analysis suggest that reflections from uniform surfaces do not affect the detection and recognition of typical indoor walls. This is in agreement with the experimental results presented in [32]. Specifically, ghost returns individuated in [32] are generated by multiple reflections and backscattering from the bright targets located outside the main beam of the antenna. With specific reference to an unknown environment, the main outcome of the 2D analysis is that a single data take from a single location is not adequate for a correct interpretation of the radar response. Multiple observations are mandatory for surfaces characterized by larger radar cross section or when extended targets are present, whose brightness is much greater than the brightness of walls.

4.3. 3D Geometry. In this section the distances associated with minimum time delay, the maximum time delay, and boresight observation are labeled as Near Range (NR_{3D}), Far Range (FR_{3D}), and Center Scene (CS_{3D}), respectively. Even though the terms are similar, these labels should not be confused with the same terms usually used in remote sensing applications and only related to the elevation plane of antenna beam.

The first example is illustrated in Figure 12 and represents a side-looking observation of the dihedral intersection edge between x-y and x-z planes, at such a distance that trihedral corner is not seen. The antennas are moving at a constant velocity $v = [0.5, 0.0, 0.0]$ (m/s) and initial position is $P_0 = [0.4, 8.0, 1.0]$ (m). The off-nadir angle is 60°. This is a particular geometrical case because only the rays emitted in the plane perpendicular to the motion and containing the line-of-sight vector $\hat{\mathbf{l}}$ can be reflected towards the antenna. All the other diverging rays are reflected away. The focused image is shown in Figure 13. As expected, there is a slight change in the distribution of energy, due to presence of backscattered energy from azimuth directions behind and ahead of the 2D observation plane along trajectory. The line of corner edge is not at FR_{3D}, even though it is very close to it. Brightest peak is closest to FR_{3D} owing to corner reflectors, layover areas, and lateral returns. It is worth noting that the capability to discriminate dihedral edges can be enhanced by the choice of millimeter wavelength, owing to typical high range resolution

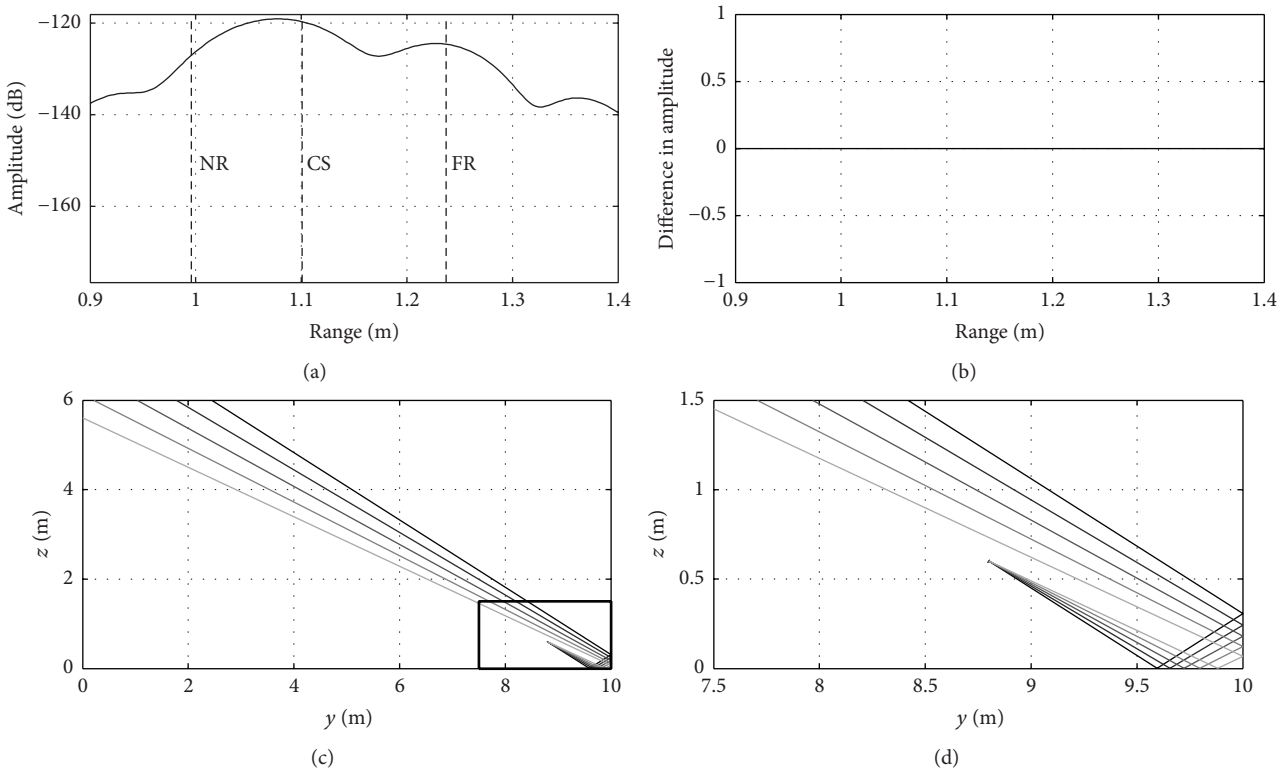

Figure 10: Case 1: observation of edge without reflections impinging on antenna. (a) Radar echoes due to backscattering only, after FFT; (b) difference between radar echoes due to both reflections and backscattering and echoes due to backscattering, after FFT; (c) ray geometry, with magnified area highlighted in black; (d) magnification of ray geometry.

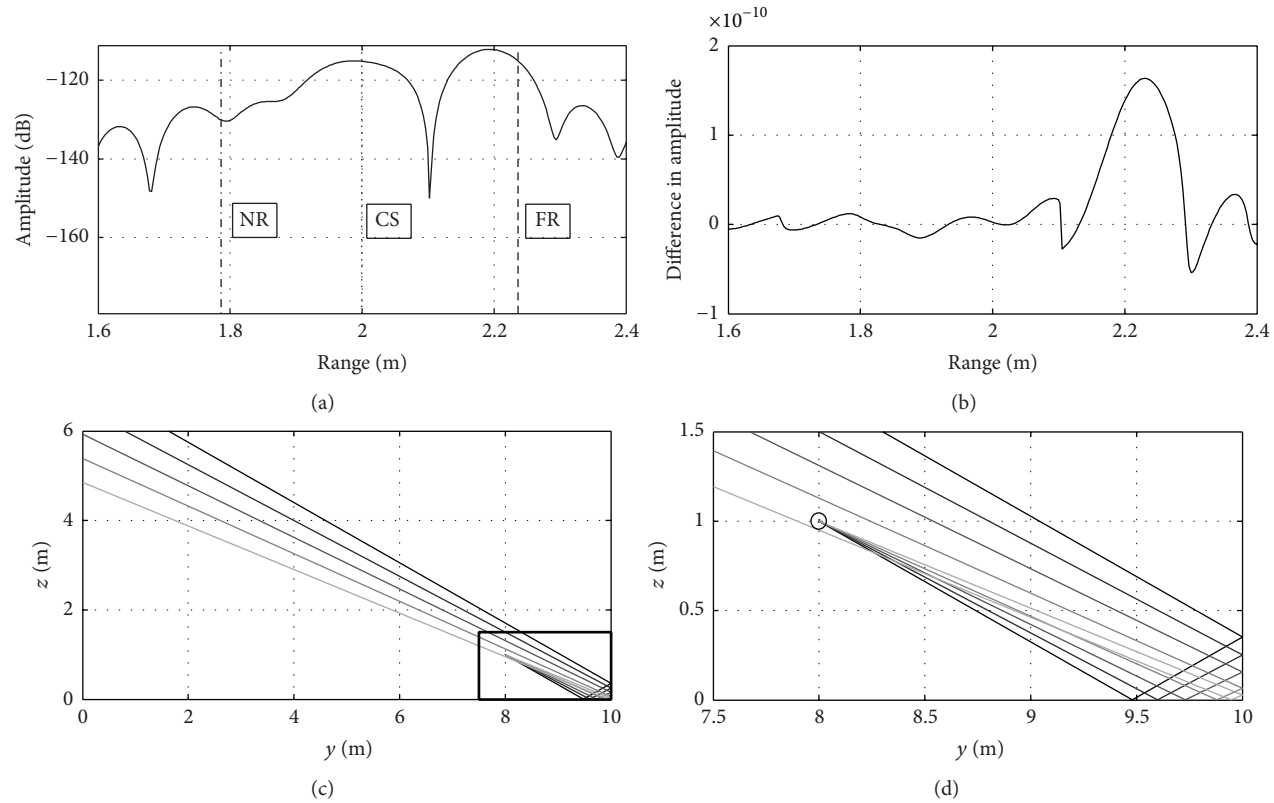

Figure 11: Case 2: observation of edge with reflected rays incident on antenna. (a) Radar echoes due to backscattering only, after FFT; (b) difference between radar echoes due to both reflections and backscattering and echoes due to backscattering, after FFT; (c) ray geometry, with magnified area highlighted in black; (d) magnification of ray geometry and position of antenna (black circle).

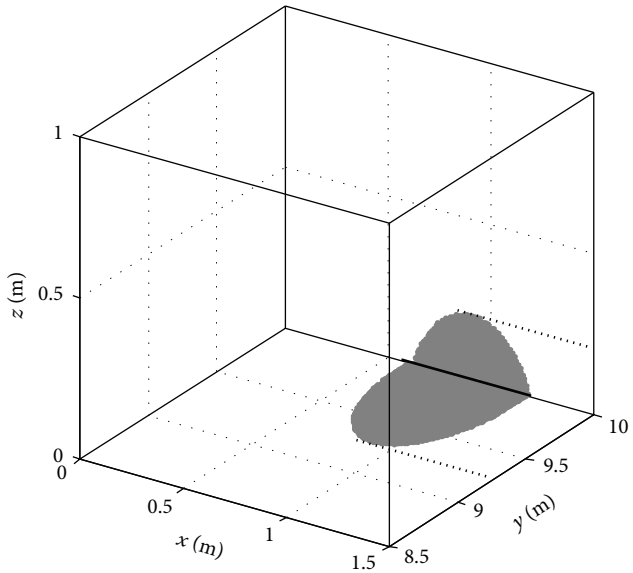

Figure 12: Dihedral corner observation. Illuminated area at a certain point and time during trajectory. Thick dotted lines indicate the illuminated areas during trajectory.

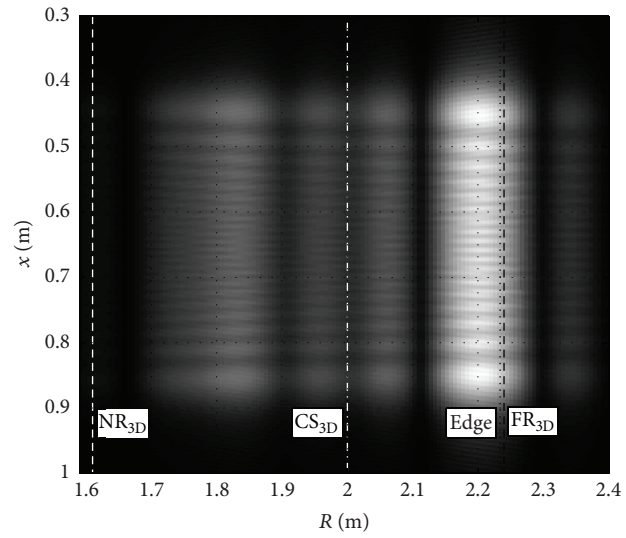

Figure 13: Focused image for dihedral corner observation.

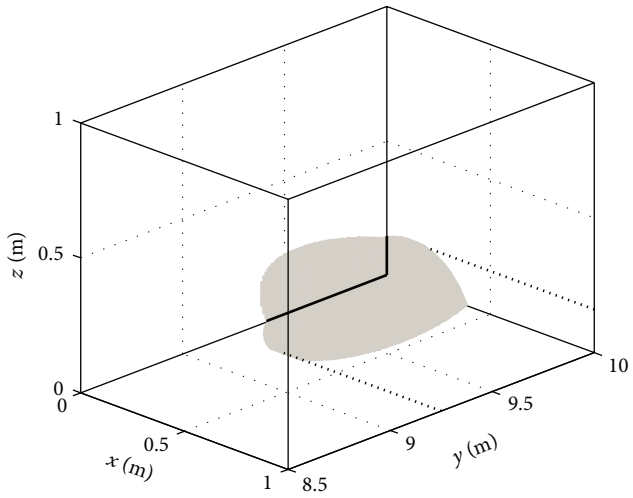

Figure 14: Trihedral corner observation. Thick black lines represent two additional edges seen during observation. Thick dotted lines indicate the illuminated areas during trajectory.

and smaller beamwidth. Indeed, even though layover cannot be removed, its effects can be reduced by illuminating a smaller area. In addition, better resolution reduces the spread of layover areas in images.

In the second example, the antennas share the same motion, starting point, and off-nadir angle with the previous case but a squint angle $\theta_{SQ} = 15^{\circ}$ is also present. Therefore, trihedral corner, obtained by intersection of planes identified by x-y, x-z, and y-z directions, is illuminated, even though not at boresight, thus simulating a more general geometry (see Figure 14). Figure 15(a) shows the range compressed matrix: the bright signature in the first 30% of integration time is due to illumination of both intersection of three walls and points affected by layover. As the antennas move away from the trihedral corner, the range signature moves as well in bins associated with larger range. Then, in the remaining part of integration interval, the signature of intersection of two walls is present. The final image, focused using the WDA algorithm, is shown in Figure 15(b). The feature generated by the dihedral illumination can be easily recognized. Moreover, a brighter horizontal line appears within different range cells, owing to the trihedral corner and the intersection edges between both x-y and y-z planes and x-z and y-z planes. Therefore, a trihedral corner reflector could be located by seeking the intersection of two orthogonal lines within the image. This is an example of information provided by the developed simulator which can be used to support the achievement of 3D awareness of the radiometric and geometric behaviors of the investigated radar sensor in indoor environment. Millimeter waves could be of benefit to reduce effects of layover even in presence of trihedral corners. The problem, however, remains and a thorough interpretation of images is necessary.

5. Conclusion

The paper presented the main features of a radar system simulator developed to support the design and the mission profile definition of a novel FMCW SAR sensor for indoor autonomous navigation and mapping by small UAS. The proposed simulator performs two main tasks, namely, the generation of the simulated environment or scene and the processing of the relevant raw SAR measurements to achieve high-resolution data. Particular attention has been devoted to the fidelity of the simulated scenes. For this reason, both nonfluctuating and fluctuating targets can be represented. In addition ray tracing techniques and three-dimensional scattering models have been implemented to

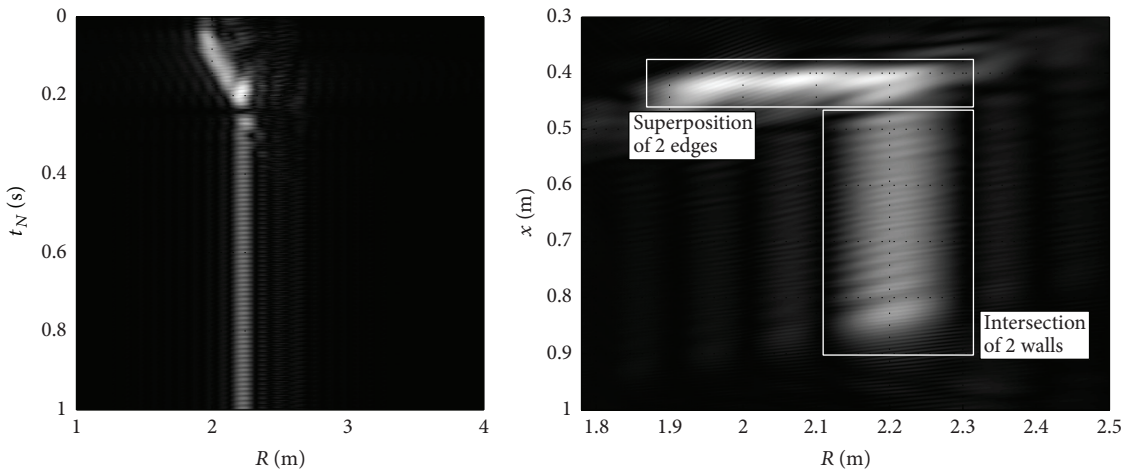

(a) Range compressed data matrix for simulation of trihedral corner

(b) Focused image for trihedral corner observation

Figure 15: Observation of trihedral corner. Focusing.

emulate the behavior of different types of surface and observation conditions. The preliminary simulation results show that when uniform walls, made of concrete, are observed multiple reflections do not play a significant role and the main geometric characteristics of an assigned control volume (e.g., dihedral and trihedral corners) can be recognized as relevant features in the focused image. It is worth noting, towards a SAR implementation on UAVs, that the simulator could help in reproducing real data from real flying paths and cope with different and complex trajectories, without loss of efficiency. The major challenge for an actual implementation is represented by main issues of real flight paths, such as attitude and acceleration variations and necessity of motion compensation. No doubt new processing techniques need to be developed in order to allow fruitful SAR implementation on UAVs. Future planned activities will deal with the simulation and analysis of more complex scenes (e.g., nonuniform radar cross section along the walls, presence of obstacles and moving targets within the control volume, or complex trajectories), the combination of multiple SAR acquisitions, and the implementation of proper techniques for automatic feature recognition and extraction. Those activities will serve as a solid base for integrating the analysis on millimeter wave FMCW SAR and developing a real system. In addition, simulations will help both the ongoing assessment of performance of a currently available commercial FMCW radar and the development of motion compensation algorithm for SAR imaging onboard UAVs.

Competing Interests

The authors declare that they have no competing interests.

Acknowledgments

This work was supported by Regione Campania within the framework of European Social Fund "P.O. Campania 2007/2013-2014/2020."

References

[1] A. F. Scannapieco, A. Renga, and A. Moccia, "Preliminary study of a millimeter wave FMCW InSAR for UAS indoor navigation," *Sensors*, vol. 15, no. 2, pp. 2309–2335, 2015.

[2] P. Rudol, M. Wzorek, G. Conte, and P. Doherty, "Micro unmanned aerial vehicle visual servoing for cooperative indoor exploration," in *Proceedings of the IEEE Aerospace Conference (AC '08)*, pp. 1–10, Big Sky, Mont, USA, March 2008.

[3] C. Micheloni, G. L. Foresti, C. Piciarelli, and L. Cinque, "An autonomous vehicle for video surveillance of indoor environments," *IEEE Transactions on Vehicular Technology*, vol. 56, no. 2, pp. 487–498, 2007.

[4] A. Ohya, A. Kosaka, and A. Kak, "Vision-based navigation of mobile robot with obstacle avoidance by single camera vision and ultrasonic sensing," in *Proceedings of the IEEE/RSJ International Conference on Intelligent Robots and Systems (IROS '97)*, pp. 704–711, IEEE, 1997.

[5] V. Degli-Esposti, F. Fuschini, E. M. Vitucci, and G. Falciasecca, "Measurement and modelling of scattering from buildings," *IEEE Transactions on Antennas and Propagation*, vol. 55, no. 1, pp. 143–153, 2007.

[6] J. Amanatides and A. Woo, "A fast voxel traversal algorithm for ray tracing," in *Proceedings of the European Computer Graphics Conference and Exhibition (Eurographics '87)*, pp. 3–10, Amsterdam, Netherlands, August 1987.

[7] R. Navarro and E. Moreno-Barriuso, "Laser ray-tracing method for optical testing," *Optics Letters*, vol. 24, pp. 1–3, 1999.

[8] R. Opromolla, G. Fasano, G. Rufino, and M. Grassi, "Uncooperative pose estimation with a LIDAR-based system," *Acta Astronautica*, vol. 110, pp. 287–297, 2015.

[9] D. Maturana and S. Scherer, "3D convolutional neural networks for landing zone detection from LiDAR," in *Proceedings of the IEEE International Conference on Robotics and Automation (ICRA '15)*, pp. 3471–3478, IEEE, Seattle, Wash, USA, May 2015.

[10] S. Auer, S. Hinz, and R. Bamler, "Ray-tracing simulation techniques for understanding high-resolution SAR images," *IEEE Transactions on Geoscience and Remote Sensing*, vol. 48, no. 3, pp. 1445–1456, 2010.

[11] T. Balz, H. Hammer, and S. Auer, "Potentials and limitations of SAR image simulators—a comparative study of three simulation approaches," *ISPRS Journal of Photogrammetry and Remote Sensing*, vol. 101, pp. 102–109, 2015.

[12] N. Peinecke, H.-U. Doehler, and B. R. Korn, "Phong-like lighting for MMW radar simulation," in *Millimetre Wave and Terahertz Sensors and Technology*, vol. 7117 of *Proceedings of SPIE*, Cardiff, UK, October 2008.

[13] L. Subrt, P. Pechac, and S. Zvanovec, "New approach to modeling of diffuse reflection and scattering for millimeter-wave systems in indoor scenarios," *PIERS Online*, vol. 8, no. 6, pp. 719–722, 2010.

[14] C. W. Trueman, R. Paknys, J. Zhao, D. Davis, and B. Segal, "Ray tracing algorithm for indoor propagation," in *Proceedings of the16th Annual Review of Progress in Applied Computational Electromagnetics (ACES '00)*, pp. 493–500, IEEE, Monterey, Calif, USA, March 2000.

[15] K. H. Ng, E. K. Tameh, and A. R. Nix, "A new hybrid geometrical optics and radiance based scattering model for ray tracing applications," in *Proceedings of the IEEE International Conference on Communications (ICC '05)*, pp. 2168–2172, May 2005.

[16] A. F. Scannapieco, A. Renga, and A. Moccia, "Compact millimeter wave FMCW InSAR for UAS indoor navigation," in *Proceedings of the 2nd IEEE International Workshop on Metrology for Aerospace (MetroAeroSpace '15)*, pp. 551–556, Benevento, Italy, June 2015.

[17] H. Griffiths, "New ideas in FM radar," *Electronics & Communications Engineering Journal*, vol. 2, no. 5, pp. 185–194, 1990.

[18] A. Meta, P. Hoogeboom, and L. P. Ligthart, "Signal processing for FMCW SAR," *IEEE Transactions on Geoscience and Remote Sensing*, vol. 45, no. 11, pp. 3519–3532, 2007.

[19] A. F. Scannapieco, A. Renga, and A. Moccia, "Performance analysis of millimeter wave FMCW InSAR for UAS indoor operations," in *Proceedings of the IEEE International Geoscience and Remote Sensing Symposium (IGARSS '15)*, pp. 806–809, Milan, Italy, July 2015.

[20] R. Sullivan, "Synthetic aperture radar," in *Radar Handbook*, M. I. Skolnik, Ed., pp. 17.1–17.37, McGraw-Hill, New York, NY, USA, 2008.

[21] J. C. Curlander and R. N. McDonough, *Synthetic Aperture Radar: Systems and Signal Processing*, John Wiley & Sons, New York, NY, USA, 1992.

[22] A. Ribalta, "High resolution SAR image reconstruction: the generalized backprojection algorithm," in *Proceedings of the IEEE International Geoscience and Remote Sensing Symposium (IGARSS '11)*, pp. 363–365, IEEE, Vancouver, Canada, July 2011.

[23] R. Bamler, "A comparison of range-Doppler and wavenumber domain SAR focusing algorithms," *IEEE Transactions on Geoscience and Remote Sensing*, vol. 30, no. 4, pp. 706–713, 1992.

[24] R. Wang, O. Loffeld, H. Nies, S. Knedlik, M. Hägelen, and H. Essen, "Focus FMCW SAR data using the wavenumber domain algorithm," *IEEE Transactions on Geoscience and Remote Sensing*, vol. 48, no. 4, pp. 2109–2118, 2010.

[25] E. C. Zaugg and D. G. Long, "Theory and application of motion compensation for LFM-CW SAR," *IEEE Transactions on Geoscience and Remote Sensing*, vol. 46, no. 10, pp. 2990–2998, 2008.

[26] A. Moccia and A. Renga, "Spatial resolution of bistatic synthetic aperture radar: impact of acquisition geometry on imaging performance," *IEEE Transactions on Geoscience and Remote Sensing*, vol. 49, no. 10, pp. 3487–3503, 2011.

[27] A. Moccia, S. Vetrella, and S. Ponte, "Passive and active calibrator characterization using a spaceborne SAR system simulator," *IEEE Transactions on Geoscience and Remote Sensing*, vol. 32, no. 3, pp. 715–721, 1994.

[28] R. G. Kouyoumjian, "Asymptotic high-frequency methods," *Proceedings of the IEEE*, vol. 53, no. 8, pp. 864–876, 1965.

[29] F. E. Nicodemus, J. C. Richmond, J. J. Hsia, I. W. Ginsberg, and T. Limperis, *Geometrical Considerations and Nomenclature for Reflectance*, U.S. Department of Commerce, National Bureau of Standards, 1977.

[30] K. Sato, H. Kozima, H. Masuzawa et al., "Measurements of reflection characteristics and refractive indices of interior construction materials in millimeter-wave bands," in *Proceedings of the IEEE 45th Vehicular Technology Conference*, pp. 449–453, Chicago, Ill, USA, July 1995.

[31] T. Teshirogi and T. Yoneyama, "Millimeter-wave propagation," in *Modern Millimeter-Wave Technologies*, pp. 127–164, Ohmsha, Tokyo, Japan, 1999.

[32] M. Moallem and K. Sarabandi, "Polarimetric study of MMW imaging radars for indoor navigation and mapping," *IEEE Transactions on Antennas and Propagation*, vol. 62, no. 1, pp. 500–504, 2014.